analytical chemistry

pubs.acs.org/ac Article

High Sensitivity Extended Nano-Coulter Counter for Detection of Viral Particles and Extracellular Vesicles

Swarnagowri Vaidyanathan,[$] Harshani Wijerathne,[$] Sachindra S. T. Gamage,[$] Farhad Shiri, Zheng Zhao, Junseo Choi, Sunggook Park, Małgorzata A. Witek, Collin McKinney, Matthew Verber, Adam R. Hall, Katie Childers, Taryn McNickle, Shalee Mog, Elaine Yeh, Andrew K. Godwin, and Steven A. Soper*

Cite This: *Anal. Chem.* 2023, 95, 9892−9900 Read Online

ACCESS | Metrics & More | Article Recommendations | Supporting Information

ABSTRACT: We present a chip-based extended nano-Coulter counter (XnCC) that can detect nanoparticles affinity-selected from biological samples with low concentration limit-of-detection that surpasses existing resistive pulse sensors by 2−3 orders of magnitude. The XnCC was engineered to contain 5 in-plane pores each with an effective diameter of 350 nm placed in parallel and can provide high detection efficiency for single particles translocating both hydrodynamically and electrokinetically through these pores. The XnCC was fabricated in cyclic olefin polymer (COP) via nanoinjection molding to allow for high-scale production. The concentration limit-of-detection of the XnCC was 5.5×10^3 particles/mL, which was a 1,100-fold improvement compared to a single in-plane pore device. The application examples of the XnCC included counting affinity selected SARS-CoV-2 viral particles from saliva samples using an aptamer and pillared microchip; the selection/XnCC assay could distinguish the COVID-19(+) saliva samples from those that were COVID-19(−). In the second example, ovarian cancer extracellular vesicles (EVs) were affinity selected using a pillared chip modified with a MUC16 monoclonal antibody. The affinity selection chip coupled with the XnCC was successful in discriminating between patients with high grade serous ovarian cancer and healthy donors using blood plasma as the input sample.

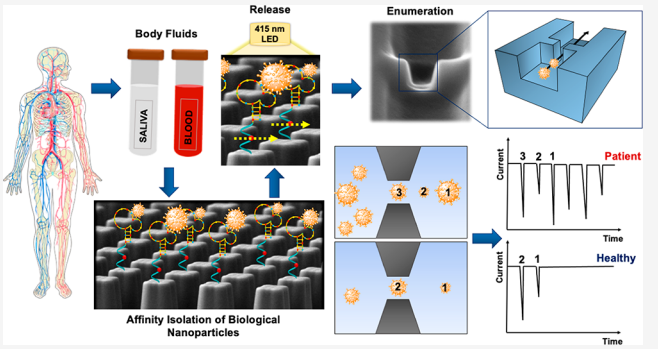

INTRODUCTION

Coulter counters or resistive pulse sensors (RPS) are based on the principle that particles driven through a narrow constriction (i.e., pore) positioned between two reservoirs containing a conductive solution will result in a transient perturbation of the pore's conductance.[1−3] Depending on the balance of the particle's charge and the conductivity of the electrolyte solution, either increases or decreases in the current flowing through the fluidic circuit can be observed. The magnitude and duration of this event are used to determine the size of the particle and its speed of travel through the pore, respectively, while the number of events per unit time correlates with the concentration of particles in the sample.[4−6] The size of the pore can be manipulated to detect different particle sizes and can range from a few micrometers (biological cells) to a few nanometers (single molecules).[7]

There are several methods for sensing biological nanoparticles such as extracellular vesicles (EVs) or viral particles (effective diameter <500 nm), including transmission electron microscopy (TEM), nanoparticle tracking analysis (NTA), flow cytometry, and RPS.[8] TEM and flow cytometry are challenging because labeling of the particles must be performed, and the required equipment and workflow can be complicated. NTA and RPS, on the other hand, negate the need for labeling and can reduce the complexity of the measurement workflow. In contrast to NTA, RPS can provide size and concentration results with lower measurement variability.[8] The challenge with RPS is that the pore size must be adjusted to accommodate the size of the particles being analyzed; the size range of particles that can be detected with respect to the pore size is ∼5-fold.[8] In addition, due to the small size of the pore, the volume throughput and sampling efficiency, which is defined as the number of targets moving into the sensing region with respect to those introduced into the measurement device and has also been referred to as the capture rate in the RPS literature, can be quite low, giving rise to modest concentration limits-of-detection (LOD).

Types of RPS Detectors. Biological nanopores typically consist of proteins embedded within a lipid bilayer that are

Received: February 25, 2023
Accepted: June 7, 2023
Published: June 19, 2023

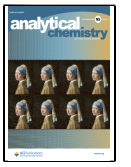

https://doi.org/10.1021/acs.analchem.3c00855
Anal. Chem. 2023, 95, 9892−9900

restricted in terms of their size (<5 nm).[9,10] Synthetic nanopores are an attractive alternative because their size, shape, and material can be carefully controlled.[11] There are two types of synthetic pores: (1) out-of-plane pores in which the pore is configured perpendicular to the fluidic elements and (2) in-plane pores in which the pore is parallel with respect to the associated fluidic network.

Pores for particle detection have used polycarbonate pores with submicron diameters to measure the size of type C coronaviruses.[12] For example, Zhou et al. used a 40 nm conical nanopore track-etched in a poly(ethylene terephthalate) membrane to identify hepatitis B virus.[13] Recently, 100 nm pores embedded within a silicon nitride membrane fabricated via TEM have been used to sense adeno-associated viruses (AAVs) and their molecular cargo.[14] All of the aforementioned solid-state pores consisted of an out-of-plane sensor with a fixed size.

In-plane pores are advantageous over out-of-plane formats because the pores can be easily integrated into a fluid network facilitating the ease of fabrication using top-down strategies, unique measurement modalities not available using out-of-plane sensors, the ability to integrate sample preparation to the RPS, and increased sample transfer of analytes to the sensing pores. For example, Sohn and team developed a PDMS-based in-plane RPS to measure single DNA molecules,[15] which were fabricated using multistage photolithography and electron beam lithography with dry etching for pattern transfer into a quartz substrate.[16] Harms et al. fabricated two pores in series in silicon and evaluated the electrophoretic mobility of HBV capsids based on the time of travel between two pores placed in series.[17] Fraikin et al. reported a nanoparticle analyzer to detect T7 bacteriophage and utilized hydraulic flow to direct the sample into a single extended nanoconstriction using a PDMS device.[18] The challenge with RPS devices is that they use a single pore, and as such, while they can detect a single particle, they show modest concentration limits-of-detection (LOD). RPS devices utilized to sense various particles are summarized in Table S1. As seen, the concentration LOD is typically >10^6 particles/mL, which is a consequence of the low sampling efficiency.

In this study, we report the use of 5 parallel extended nanopores (~350 nm effective diameter each) fabricated in cyclic olefin polymer (COP) via nanoinjection molding. We utilized photolithography to fabricate microchannels, followed by focused ion beam (FIB) milling to produce extended nanopores in a Si master. The features from the Si master were then transferred to COP through an intermediate UV-curable resin using the high-scale production technique of nanoinjection molding.[19] The use of the intermediate resin stamp accommodated the prototyping of several design iterations without requiring the production of metal molding tools via electrodeposition.

Our overall goal was to detect biological particles having diameters ranging from 40 to 350 nm using an XnCC (extended nano-Coulter counter) with sufficient concentration LOD to span the entire clinical concentration range required for biological nanoparticle measurements; for example, SARS-CoV-2 viral particles in clinical saliva samples can range from 500 to 10^8 viral particles/mL.[20] We have reported the use of a single extended nanopore device fabricated via nanoimprint lithography in COP with a concentration LOD of 5.8×10^6 particles/mL,[21] but due to its poor concentration LOD, we opted for an XnCC device possessing 5 pores in parallel to increase the sampling efficiency to allow for the detection of particles at low concentrations. We tested the performance and fluid dynamics of the optimal design by using COMSOL simulations and conducted experimental measurements to verify our simulation results. Furthermore, the analytical figures-of-merit were secured by using the optimal XnCC design. The XnCC device was then used in two applications: (i) detection of SARS-CoV-2 viral particles from saliva samples and (ii) detection of EVs from plasma samples of patients with ovarian cancer. In both applications, the biological particles were surface affinity selected using a pillared microfluidic chip[22] followed by release of the surface-captured particles using a photocleavable linker[23] and subsequently enumerated using the high sensitivity XnCC device.

MATERIALS AND METHODS

XnCC Fabrication. The XnCC device was fabricated using nanoinjection molding (see Figure S1). However, because the startup time and cost for injection molding is high due to the need for generating Ni mold inserts via electrodeposition,[19] we opted for an alternative protocol by making an intermediate resin mold insert to forego the need for a Ni plating step during the prototyping stages of device development.[24] We briefly describe those steps in the Supporting Information, which involved making a Si master from which resin stamps were produced.

Fluorescence Measurements. Fluorescence measurements using a wide-field illumination microscope and a dye tracer were used to check proper XnCC device cover plate sealing and that the in-plane pores were not deformed. See the Supporting Information for a description of these measurements.

COMSOL Simulations. The fluidic operation of the XnCC device was modeled using COMSOL. Please see the Supporting Information for a description of the conditions used for these simulations.

Scanning Electron Microscopy (SEM). SEMs of the thermoplastic microfluidic/nanofluidic devices and resin stamps were acquired using a Hitachi FlexSEM 1000 II SEM. The thermoplastic devices were sputter coated with a 10 nm conductive Au layer prior to SEM using a Denton Desk II Sputter Coater. SEM images of the Si mold master were acquired using a Quanta 3D DualBeam FEG FIB-SEM (FEI).

Transmission Electron Microscopy (TEM). Please see the Supporting Information for information about the methodology adopted for acquiring TEM images.

Nanoparticle Tracking Analysis (NTA). Please see the Supporting Information for additional information about the NTA conditions.

Healthy Donor and Patient Testing for COVID-19 and HGSOC. For information on the recruitment of patients and healthy donors for testing of the particle selection and XnCC testing, please see the Supporting Information.

RESULTS AND DISCUSSION

We preliminarily evaluated three different XnCC designs with one consisting of a single in-plane pore and two with 5 parallel in-plane pores (see Figures S2, S3, and S4). XnCC design iterations, COMSOL simulations, and experimental results (see the Supporting Information) provided insights into the design configuration required to improve the sampling efficiency to lower the concentration limit-of-detection: (i)

https://doi.org/10.1021/acs.analchem.3c00855
Anal. Chem. 2023, 95, 9892−9900

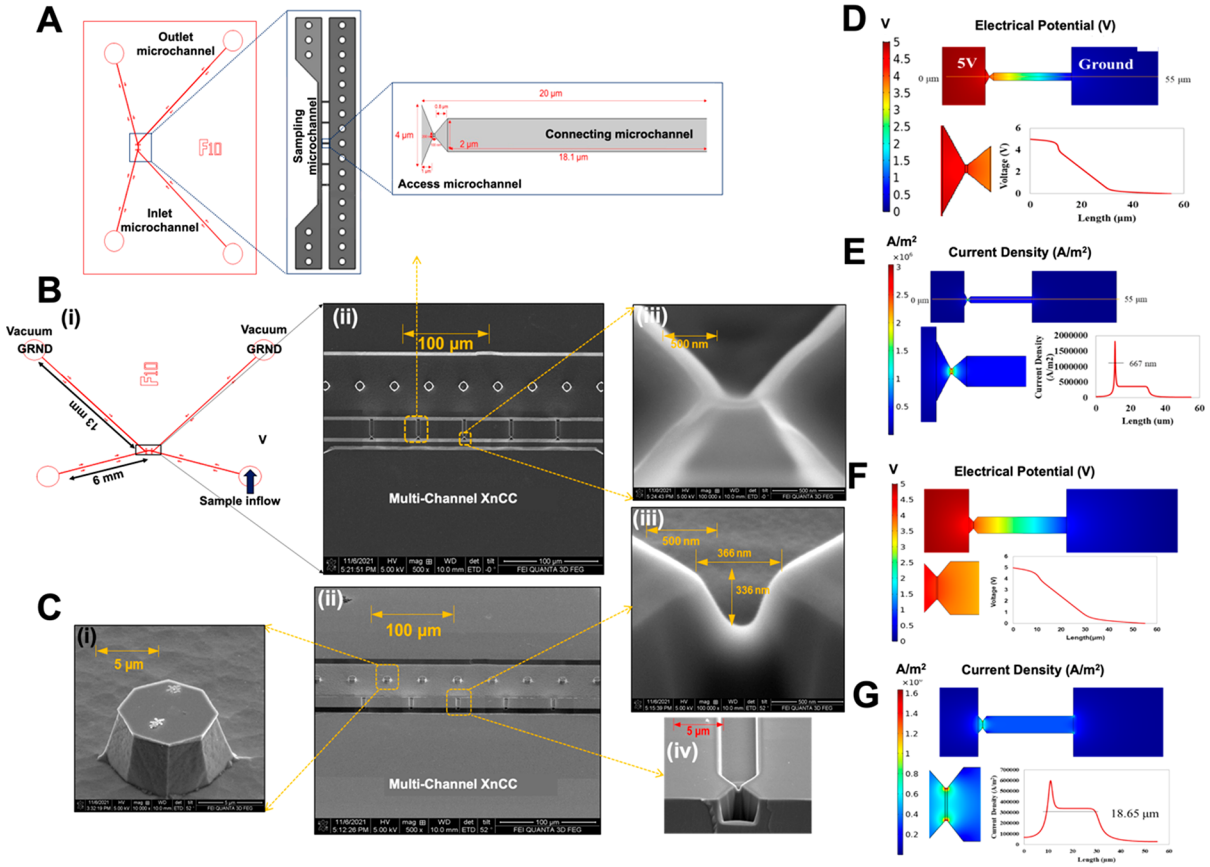

Figure 1. (A) Grayscale diagram of a single in-plane nanopore associated with the optimal XnCC design. The extended in-plane nanopore was placed adjacent to the access microchannel and the funnel structure near the pore was 4 μm and the connecting channel was 2 μm to have a higher injection efficiency of the particles into the XnCC. V = applied DC bias voltage, and GRND = grounding reservoirs. (B) Schematic of the entire XnCC device containing the 5 in-plane pores (i). SEM of the 5 in-plane nanopores FIB milled into the Si master. The width of the access microchannels on the sample side was reduced from 25 to 10 μm only in the region having the XnCC in-plane pores (ii). Also included is a top-down SEM of the Si master under a higher magnification of the in-plane pore (iii). (C) SEMs of the injection molded device from the resin stamp showing the support pillar used on the vacuum side of the device (i), a low magnification view of the sensing region of the device (ii), the single pore at 52° tilt view (iii), and the input 4 μm funnel (iv). (D) COMSOL simulations of the 350 nm effective diameter pore showing the electric potential (−5 V). Also shown is a magnified image of the XnCC and the corresponding line plot showing the 5 V drop across the fluidic circuit. (E) COMSOL simulation of the current density corresponding to the potential drop shown in (D) with the regions in the XnCC having a higher current density. Included is a magnified image of the XnCC with the corresponding line plot of the current density. The current density plot of the XnCC gave rise to an effective length of 665 nm. (F) Potential drop across the 5 XnCC in-plane extended nanopore sensor. A 2-dimensional line plot of potential drop versus distance across one of the XnCC in-plane extended nanopore sensors. The potential drop across the XnCC represents 10% of the total voltage drop across the sensor (5.0 V). (G) Current density profile plotted from the voltage profile to estimate the effective length of the pore at fwhm, which is 18.65 μm for a pore width of 1.75 μm.

utilize multiple pores in parallel; (ii) reduce the width of the sampling microchannel near the pores and place the pores close to the sampling microchannel; (iii) high pressure drop across the pores; (iv) utilize a 3D tapered funnel to extend the electric field further into the sampling microchannel to electrophoretically draw particles into the in-plane pores;[25] and (v) utilize an optimized forward hydraulic flow. The design iterations shown in the Supporting Information led us to the optimized design, as discussed below.

Rationale behind 5 Pores in Parallel. The selection of 5 pores was used to improve the sampling efficiency for particles while at the same time maintain a high detection efficiency of single particles when resident within the effective sampling volume. The final design had a pore size of 350 nm (effective diameter, which is equal to the mean of the pore actual dimensions, 336 nm × 366 nm), and hence, the following calculations were based on this dimension (see Figure 1 for the layout of the 5-pore device). There are two ways to achieve a sampling pore size of 5 × 350 nm: (i) a single pore of 1,750 nm effective diameter (d_{eff}) or (ii) fabricating 5 pores in parallel with each pore having an effective diameter of 350 nm. From our experiments using 1× PBS, the open pore current at 5 V applied across a single 350 nm (d_{eff}) pore was ~30 or 150 nA for case (ii) devices (5 × 30 nA = 150 nA as measured with these devices), and for the case (i) device, the open pore current would also be 150 nA. From Ohm's law, the total resistance of a single 350 nm pore was determined to be 200 MΩ. For an average particle diameter of 150 nm, the occlusion volume, OV (V_p/V_{det}; V_p = particle volume and V_{det} = effective pore sensing volume), for case (ii) is 2.8%, and for case (i), OV = 3.9 × 10^{-3} %. V_{det} was calculated based on h_{eff} (effective sampling zone length) determined using current density plots (fwhm is defined as the half-width of the current density function from the current excursion from the baseline to its end, which includes the narrow peak shape atop the trapezoid) and the applied electric field drop across the pore.[18] The

https://doi.org/10.1021/acs.analchem.3c00855
Anal. Chem. 2023, 95, 9892−9900

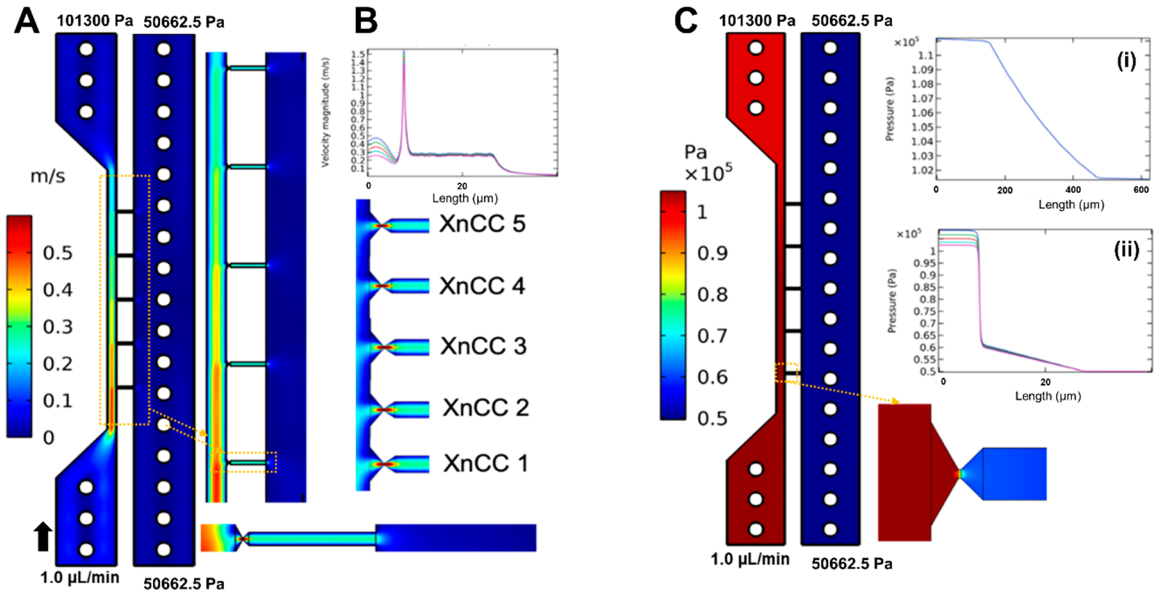

Figure 2. COMSOL simulation of hydrodynamic operation of the 5-pore XnCC device. (A) The velocity profile with the inlets set to atmospheric pressure on one side of the inlet and the other side set to operate at a volumetric flow rate of 1 μL/min. The outlets were set to a pressure of 50,000 Pa (estimated from the pressure sensor). The fluid from the inlet side enters the outlet side due to the differences in the pressure drop created by the vacuum pump. (B) Magnified image showing the higher velocity near the in-plane extended nanopores with a line graph showing the velocity profiles across all 5 in-plane extended nanopores. The effective sampling zone is defined by the 10 μm wide channel region adjacent to the 5 in-plane pores. (C) Pressure drops across the 5 in-plane extended nanopores and inlet microchannel network. (i) The pressure drop in the inlet microchannel showing a small pressure drop of 10 kPa. (ii) The pressure drop across the in-plane extended nanopores and the connecting microchannel showing the majority of the pressure drop occurring across the in-plane pores. The black arrow indicates the flow direction of the carrier electrolyte.

connecting microchannel (2 μm in depth and width) is 5.7 times greater in size than the 350 nm (d_{eff}) pore (see Figure 1A; SEMs of the fabricated device can be found in Figure 1B,C). In this case, the electric field drop is restricted to the in-plane pore (Figure 1D,E). Figure 1E shows the corresponding current density for case ii, giving h_{eff} = 667 nm compared to a single 1.75 μm pore with h_{eff} = 18.65 μm (Figure 1F,G). The corresponding probe volume for case (i) is 44.8 aL, while for case (ii) each pore gives a probe volume of 64.4 zL yielding a total volume for the 5 pores of 322 zL. We should note that the design length of the pores was 100 nm.

The measurable signal, ΔI, can be estimated from $\Delta I \approx I_T \times$ OV, where I_T is 150 nA (open pore current for the 5-pore device and 1× PBS with V = 5 V). For a single 150 nm particle moving through either a single 350 nm pore in the 5-pore case (ii) or through the 1,750 nm pore for case (i), ΔI would be 82.5 and 5.85 pA, respectively, and there would be a normalized amplitude response ($\Delta I/I_T$) of 0.55 and 0.39, respectively. Therefore, splitting the effective sampling volume for RPS into smaller pores (array of 5 pores in parallel) as opposed to a single pore of the same effective diameter can increase the signal-to-background ratio in the measurement. In addition, the net increase in volume throughput scales linearly with the number of pores in the array.

Design Schematic and SEM Images. The XnCC having 5 pores placed in parallel was designed to have similar dimensions for each pore (Figure 1B) with FIB milling used to produce the in-plane extended nanopores [width and depth of 366 and 336 nm, respectively, with d_{eff} = 350 nm (Figure 1C(iii))]. The width of the access microchannels was 25 μm (width and depth), but in the region near the 5 pores (i.e., sampling microchannel), the channel was reduced to 10 μm (Figure 1B(ii)) to increase the sampling efficiency, defined as the number of particles per unit time traveling through the in-plane pores (Figure 1A) with respect to the total number of particles traveling through the sampling microchannel. In the optimized design we positioned the in-plane pores next to a 4 μm 3D tapered funnel to further increase the sampling efficiency by extending the electric field into the sampling microchannel.[25] An SEM image of the funnel and the XnCC can be seen in Figure 1C(iv).

COMSOL Simulations of the Hydrodynamic Operation of the XnCC. We used a combination of electrokinetic and hydrodynamic flow to affect the fluidic operation of the XnCC. Hydrodynamic flow was used to bring particles to the XnCC sampling region, which was defined as the 10 μm wide microchannel adjacent to the in-plane pores (see Figure 2A), and vacuum pressure pulling particles through the pores. COMSOL simulations were performed on the optimized XnCC design having pores of 350 nm × 100 nm (w × l) with conditions at the inlet having a 1 μL/min volume flow rate. The outlet vacuum channel was held at 50 kPa. The particle velocity in the microchannel ranged from 0.1 m/s in the wider part of the microchannel (near the inlets) to 0.25 m/s in the sampling region, which was placed in front of the in-plane pores (Figure 2A). The velocity through the 5 in-plane pores indicated that they were uniform, reaching a velocity of 1.5 m/s (Figure 2B), which would give a pulse duration of 0.45 μs. The pressure profile (Figure 2C) showed a drop in pressure between the sampling microchannel (i) and the outlet microchannel (ii); Figure 2C(i) shows the pressure drop across the inlet microchannel. Most of the pressure drop (~40 kPa) occurred across the in-plane pores with a ~10 kPa pressure drop in the connecting channel placed after the extended in-plane nanopores (Figure 2C(ii)).

https://doi.org/10.1021/acs.analchem.3c00855
Anal. Chem. 2023, 95, 9892−9900

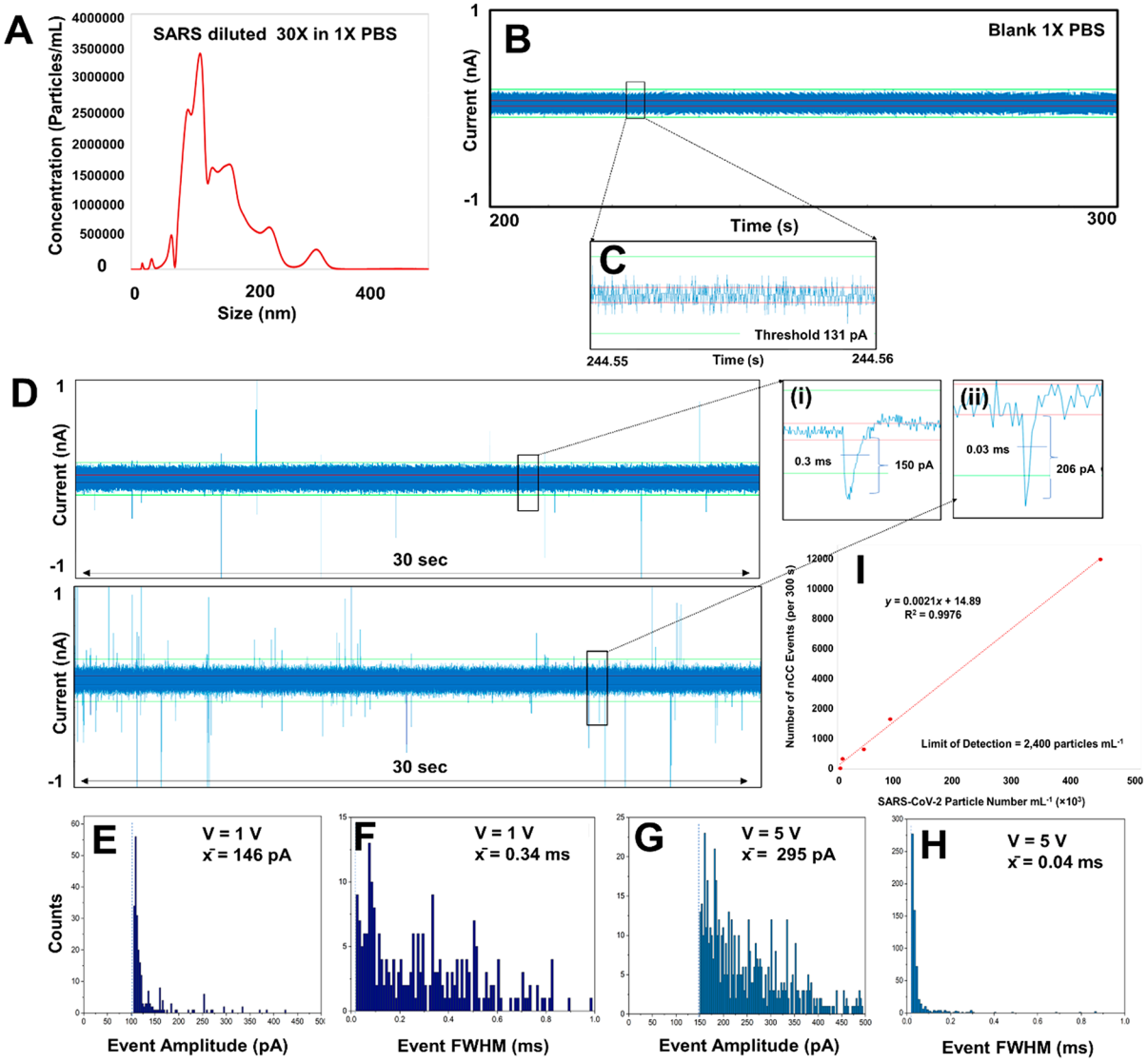

Figure 3. (A) NTA results of SARS CoV-2 VPs showing the size distribution of the particles. (B) Processed RPS data for the negative control, which consisted of 1× PBS with no apparent events crossing the threshold. (C) Expanded view of the 1× PBS data trace for a time duration of 0.01 s. (D) Representative data trace for 52,000 VPs/mL seeded into 1× PBS with events shown for a 30 s time interval and a 1 V bias (upper panel) and 5 V bias (lower panel). (i) Expanded view of a RPS event for a negative polarity peak at 1 V showing a peak amplitude of 150 pA and a half-width of 0.3 ms. (ii) Expanded view of a negative polarity event having an amplitude of 206 pA and a half-width of 0.03 ms for the 5 V RPS data. (E) Histogram showing the distribution of peak amplitudes with an average peak amplitude of 146 pA at 1 V. (F) The dwell time half-width distribution of events for a bias voltage of 1 V with an average half-width of 0.34 ms. (G) Histogram showing the distribution of peak amplitudes with an average peak amplitude of 295 pA using an applied voltage of 5 V. (H) The dwell time half-width distribution of events with an average half-width of 0.04 ms for an applied voltage of 5 V. The dashed line shows the threshold applied to the histogrammed data. (I) Calibration curve for SARS-CoV-2 seeded into 1× PBS. The LOD was calculated from this calibration curve using the slope and intercept of the linear function fit to this data at 3× the standard deviation in the RPS data. The data was sampled at 150 kHz and subjected to a 10 kHz low pass filter (see Figure S8) and 400 Hz high pass filter.

Selection of Thermoplastic for the XnCC. Using fluorescent beads, we determined that COP with a COC cover plate provided minimal amounts of nonspecific adsorption compared to PMMA/COC devices (see Figure S5). Thermoplastics not only offer the ability to be produced in a high production mode using injection molding, but they also have favorable surface chemistries for microfluidic applications.[26,27] For example, COP (see Figure S6A) can be UV/O_3 activated to make it more wettable compared to the native form of the material, which can minimize bubble formation, generate a stable electroosmotic flow (EOF), and reduce nonspecific adsorption artifacts. UV/O_3 activated plastic surfaces also create surface carboxylic acid groups to generate a higher EOF compared to the native form of the plastic (Figure S6B). While PDMS shows rapid hydrophobic recovery, many thermoplastics show minimal water contact angle changes (30° → 38°) over a 25-day period as seen in Figure S6C.

Forward Flow Rate Effects on Capture Rate. We ran a SARS CoV-2 particle suspension (2.6×10^6 particles/mL) through the XnCC chip at various volume flow rates to determine the optimal hydraulic flow to maximize the particle capture rate. It was found that the number of events at 1 μL/min was higher compared to other flow rates (see Figure S7).

https://doi.org/10.1021/acs.analchem.3c00855
Anal. Chem. 2023, 95, 9892−9900

At forward velocities <1 μL/min, a small number of particles are being swept into the sampling microchannel per unit time and are unable to keep up with the rate at which they are being drawn into the in-plane pores. However, at forward velocities >1 μL/min, the speed at which the particles travel through the sampling microchannel is such that their capture rate decreases.

Applied Voltage Effects on Event Characteristics. From the experimental results secured above, we chose SARS CoV-2 particle XnCC detection using a forward flow rate of 1 μL/min and a vacuum pump simultaneously withdrawing fluid to evaluate the performance of the XnCC possessing d_{eff} of 350 nm and 5 in-plane pores placed in parallel. In these experiments, heat-inactivated SARS-CoV-2 particles were seeded into 1× PBS (pH = 7.4). Figure 3A shows a nanoparticle tracking analysis (NTA) of the viral particles, which indicated a mean particle size of 143.7 ± 5 nm and all particles having sizes <350 nm.

We determined the average width of the current transient events at half-height and the average event amplitudes at voltages of 1 and 5 V. For these measurements, the current transients were measured using an in-house built current transimpedance amplifier (TIA) with the XnCC containing Ag/AgCl electrodes for recording electrical signals at the appropriate applied voltage.[28] Figure 3B shows a representative RPS data trace distributed over 100 s in 1× PBS blank and in Figure 3C is shown an expanded region (0.01 s); applied voltage = 1 V. An event was scored only if it had >1 data point per peak, an amplitude greater than a selected threshold, and a half-width ≥0.02 ms. As seen, the 1× PBS buffer resulted in no events exceeding the threshold.

We next seeded 52,000 SARS-CoV-2 particles/mL into the 1× PBS buffer and searched for events elicited by the XnCC for a 300 s counting interval (see Figure 3D for a 30 s span) and an applied voltage of 1 V (upper trace) and 5 V (lower trace). A threshold level was set with respect to the open pore current to reduce the false positive rate to 0 over the 300 s counting interval. Events having both positive and negative polarities were observed for both applied voltages. Expanded time-scale traces are shown in Figure 3D: (i) a negative event having an amplitude of 150 pA with a half-width of 0.3 ms (1 V) and (ii) a negative event having an amplitude of 206 pA with a half-width of 0.03 ms (5 V). A positive pulse arises from the local modulation of the ionic concentration, where the surface charge of the particle adds to the existing ionic concentration and causes an increase in the in-plane pore conductance.[29,30] In the case of negative polarity peaks, a volume exclusion process induced a lower pore conductance compared with the open pore. The occurrence of both positive and negative polarity events in our RPS trace data indicates a disparity in particle surface charge and possibly porosity of the enveloped particle.

The peak amplitude histogram (Figure 3E) showed an average amplitude of 146 pA (V_{bias} = 1 V). The event width (fwhm) or dwell time ranged from 0.03 to 1.1 ms (Figure 3F) with an average half-width of 0.34 ms and an average width of events at the base 1.27 ms indicating the sampling frequency is sufficient (34 data points for a 0.34 ms half-width and 127 data points for a 1.27 ms event) to minimize signal aliasing. However, with the bandwidth of the electronics being set to 10 kHz, some perturbation in peak shape with a fwhm <0.1 ms could occur.

Because SARS CoV-2 particles have a negative zeta potential,[31] the applied voltage was increased from 1 to 5 V to potentially increase sampling efficiency. The average peak amplitude at 5 V was estimated to be 295 pA (Figure 3G) with an average fwhm of 0.04 ms (Figure 3H). Compared to the 1 V data, there was a reduction in the average fwhm of events from 0.34 to 0.04 ms. This was attributed to the higher bias voltage, which induced a higher electrophoretic force that caused the particles (negatively charged) to translocate faster through the in-plane pores.[31] In addition, we found that the event frequency increased from 72 to 123 events with a higher bias voltage.

From the voltage dependence data, several conclusions about the particle translocation through the in-plane COP pores can be surmised: (i) Because a negative applied voltage with respect to ground was applied at the terminal end of the inlet microchannel, electrophoretic forces cause the particles to be more efficiently injected into the pores. As noted above, the event frequency increased with higher voltage when operated under identical conditions. (ii) While there is a relatively high EOF for COP/COC devices when UV/O_3 treated for ∼12 min and because the particles are moving in the opposite direction of the EOF, the electrophoretic mobility is larger than the EOF (∼1.4×10^{-5} $cm^2/(V\ s)$). The large pressure drop across the pores also assists in transporting the particles through the pore. The dwell times (i.e., peak widths) also were reduced when operating at a higher applied voltage. (iii) As seen in our data, the current transient amplitudes were voltage dependent even though there is a large hydrodynamic transport acting on the particles.

Analytical Figures-of-Merit of the XnCC. To determine the concentration LOD of the optimized XnCC design, we generated a calibration plot using 1× PBS solutions spiked with heat inactivated SARS-CoV-2 viral particles of different concentrations. The calibration curve (Figure 3I) was built from the average number of events observed over a defined counting interval (300 s) and an applied voltage of 5 V. As can be seen from the calibration plot in Figure 3I, a linear correlation was seen (R^2 = 0.9976). The concentration LOD was estimated to be 5.5×10^3 particles/mL with a sampling efficiency of 1.6×10^{-2} %, which was determined from the concentration of the viral particles, the volume flow rate, the duration of the measurement, and the number of events detected (assuming 100% detection efficiency). The concentration LOD improved from 6×10^6 particles/mL using the single pore device to 5.5×10^3 particles/mL in the device reported herein due to increases in the sampling efficiency arising from the design changes. Overall, there was a 1,100-fold improvement in the concentration LOD with our optimized design compared to the single pore device.[21]

Selection and Enumeration of SARS-CoV-2 in COVID-19 Negative and Positive Saliva Samples. Saliva samples were tested in an approved COVID-19 testing center using RT-qPCR (FDA-approved protocol). Of the 10 samples, 5 were COVID-19(−) and 5 were COVID-19(+). Before doing the XnCC enumeration, we enriched the SARS-CoV-2 particles using an affinity-enrichment microfluidic chip, which consisted of a pillared chip (see Figure S9).

A DNA aptamer was used as the affinity agent (K_d = 5.8 nM)[32] targeting the ACE2 receptor binding domain (RBD) of the spike protein of SARS-CoV-2.[33] For the covalent attachment of the aptamer to the selection chip's surface, we used a photocleavable (PC) 7-amino coumarin heterobifunc-

https://doi.org/10.1021/acs.analchem.3c00855
Anal. Chem. 2023, 95, 9892−9900

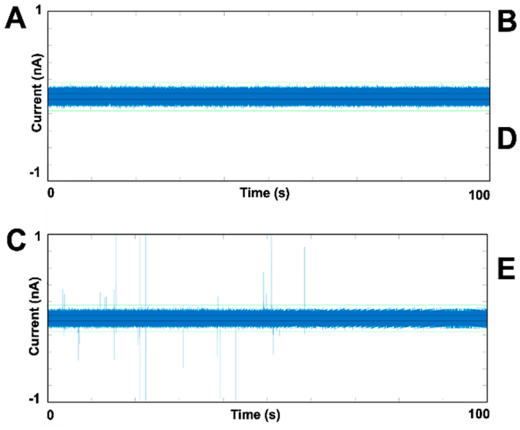

B

ID	Dominating variant at time of testing	Counting interval (s)	Number of events detected
1	Omicron BA.2	100	None
2		100	None
3		100	None
4		100	None
5		100	None

D

Dominating variant at the time of testing	COVID-19 positive sample	Counting interval (s)	Number of events detected	Event characteristics	
				Height (pA)	Half-Width (ms)
Variant Delta/Lineage B.1.617.2 (July 2021)	6	100	38	360 ± 584	0.027 ± 0.01
	7	100	245	271 ± 136	0.045 ± 0.078
	8	100	24	380 ± 197	0.029 ± 0.018
	9	100	14	243 ± 122	0.069 ± 0.0001
	10	100	12	316 ± 103	0.04 ± 0.01

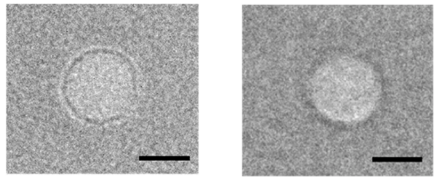

Figure 4. XnCC enumeration of viral particles enriched from clinical saliva samples. (A) RPS trace data for a COVID-19(−) saliva sample. The status of the patient was verified by using RT-qPCR. (B) Table showing the RPS event number from clinical saliva samples known to be COVID-19(−). At the time of collection, the dominant variant was known to be Omicron BA.2; this variant could be enriched using our aptamer chip. (C) RPS trace data for a COVID-19(+) patient, as deduced via RT-qPCR. (D) Table showing the number of RPS events detected during a 100 s counting interval using the XnCC chip. (E) TEM images for SARS-CoV-2 particles that were taken from the stock solution (left) and those that were enriched using the selection chip and photoreleased from the selection chip's surface (right). The scale bars represent 100 nm.

tional linker.[34] The use of this photocleavable linker allowed for the specific surface capture/enrichment of the virus particles and then blue light release from the surface intact viral particles to allow for their enumeration via the XnCC.

As seen in Figure 4A,B, the COVID-19(−) saliva samples generated no discernible signals in the XnCC RPS data traces. This resulted from the high specificity afforded by the selection chip and its affinity agent.[35] As seen from the data shown in Figure 4C,D, we successfully identified all COVID-19(+) samples using our affinity selection chip and the XnCC. TEM images of the captured and released SARS-CoV-2 virions can be seen in Figure 4E. The SARS-CoV-2 particles taken from the stock solution and those that were sent through the capture and subsequent release assay did not seem to induce damage in the particles. We also carried out NTA analysis on the stock solution of the SARS-CoV-2 particles and those that were selected and released and also noted no change in the size distribution of the particles (data not shown).

High Grade Serous Ovarian Cancer (HGSOC) EV Selection and Enumeration. To evaluate the feasibility of using the selection and XnCC chips for sampling EVs from plasma samples, high-grade serous ovarian cancer patients and healthy donors were analyzed using an anti-MUC16 monoclonal antibody modified selection chip, and following capture, the recovered particles were photoreleased and analyzed using the XnCC device. A typical RPS trace of EVs is shown in Figure S10A. As seen, both negative and positive polarity events were detected, as we noted for SARS-CoV-2. TEM images of selected and released EVs from HGSOC plasma samples are shown in Figure S10B, and NTA indicated an average particle size of ∼133 nm (see Figure S10C). From Figure S10D, the samples were placed into one of two groups and labeled as HGSOC vs healthy donors based on the number of EVs detected using the XnCC. The two groups showed a significant difference (p = 0.0007); the higher EV concentration group was assigned to those with HGSOC.

CONCLUSIONS

Highly accessible screening tests are sorely needed in several healthcare scenarios, especially those that can be implemented at the point-of-care. For example, in the case of COVID-19 home testing is an essential tool for effective containment of COVID-19 because it allows for more frequent testing and provides rapid results as opposed to clinical testing.[36] While new at-home technologies for screening based on PCR or antigens have evolved, there are some challenges, such as the need for cold storage due to the use of sensitive reagents.

To address these challenges, we presented a technology to identify those that have been infected with SARS-CoV-2. Unique to our technology is the ability to select intact SARS-CoV-2 from a non-invasively acquired sample (saliva) and perform label-free counting of the particles (see Figure 4E). The XnCC and selection chips were made from a thermoplastic and could be fabricated by injection molding that is conducive to high-scale production, making it appropriate for large-scale screening tests.

Because many RPS devices may not provide a concentration LOD (see Table S1) that would cover the entire clinically relevant range (for SARS-CoV-2 in saliva samples, range = 10^2−10^8 particles/mL),[20] we developed a 5-pore XnCC device with the proper fluidic interface to improve the sampling efficiency and, consequently, the concentration LOD. The XnCC device provided analytical figures-of-merit competitive to PCR-based testing with a concentration LOD of 5.5×10^3 particles/mL. If one considers a 10-fold enrichment by the selection chip (300 μL → 30 μL), the effective LOD is 550 particles/mL for the selection/XnCC assay.

The challenge with RPS is the universal nature of detection meaning that any particle can be detected as long as it satisfies a size criterion.[21] Therefore, when processing complex biological samples preselection of targets is required before enumeration. In this work, we used a selection chip to affinity select EVs (anti-MUC16 mAbs) or viral particles (51 nt aptamer) from complex clinical samples. We are currently packaging the selection and XnCC chips onto a fluidic motherboard to develop an integrated and modular system.[37−39]

Finally, in the present manuscript we discussed the use of 5 in-plane pores to increase the sampling efficiency resulting in an improvement of the LOD. We are currently working on a new sensor format in which 25 in-plane pores are utilized. In this configuration, the pores are grouped in a set of 5 with each

https://doi.org/10.1021/acs.analchem.3c00855
Anal. Chem. 2023, 95, 9892−9900

grouping monitored by a single channel of a 5-channel TIA. In this way, we will be able to do multiplexing (i.e., 5-plex) or increase the sample throughput compared to the 5-channel device reported herein. We are also developing methods to quantify the single-particle detection efficiency using our multipore system by coupling the RPS readout with high frame rate fluorescence readout with labeled nanoparticles to determine whether we can increase the number of pores in parallel transduced using a single-channel TIA without negatively affecting single-particle detection efficiency.

■ ASSOCIATED CONTENT

Supporting Information

The Supporting Information is available free of charge at https://pubs.acs.org/doi/10.1021/acs.analchem.3c00855.

Supporting figures and table, experimental methods, and results and discussion (PDF)

■ AUTHOR INFORMATION

Corresponding Author

Steven A. Soper − *Bioengineering Program, Department of Chemistry, Center of BioModular Multiscale Systems for Precision Medicine, and Department of Mechanical Engineering, The University of Kansas, Lawrence, Kansas 66045, United States; KU Comprehensive Cancer Center and Kansas Institute for Precision Medicine, University of Kansas Medical Center, Kansas City, Kansas 66160, United States;* orcid.org/0000-0002-8292-7058; Email: ssoper@ku.edu

Authors

Swarnagowri Vaidyanathan − *Bioengineering Program and Center of BioModular Multiscale Systems for Precision Medicine, The University of Kansas, Lawrence, Kansas 66045, United States*

Harshani Wijerathne − *Department of Chemistry and Center of BioModular Multiscale Systems for Precision Medicine, The University of Kansas, Lawrence, Kansas 66045, United States*

Sachindra S. T. Gamage − *Department of Chemistry and Center of BioModular Multiscale Systems for Precision Medicine, The University of Kansas, Lawrence, Kansas 66045, United States;* orcid.org/0000-0002-7507-3226

Farhad Shiri − *Department of Chemistry and Center of BioModular Multiscale Systems for Precision Medicine, The University of Kansas, Lawrence, Kansas 66045, United States*

Zheng Zhao − *Bioengineering Program and Center of BioModular Multiscale Systems for Precision Medicine, The University of Kansas, Lawrence, Kansas 66045, United States*

Junseo Choi − *Center of BioModular Multiscale Systems for Precision Medicine, The University of Kansas, Lawrence, Kansas 66045, United States; Mechanical & Industrial Engineering Department, Louisiana State University, Baton Rouge, Louisiana 70803, United States;* orcid.org/0000-0002-3461-3820

Sunggook Park − *Center of BioModular Multiscale Systems for Precision Medicine, The University of Kansas, Lawrence, Kansas 66045, United States; Mechanical & Industrial Engineering Department, Louisiana State University, Baton Rouge, Louisiana 70803, United States*

Małgorzata A. Witek − *Department of Chemistry and Center of BioModular Multiscale Systems for Precision Medicine, The University of Kansas, Lawrence, Kansas 66045, United States*

Collin McKinney − *Department of Chemistry, University of North Carolina, Chapel Hill, North Carolina 27514, United States*

Matthew Verber − *Department of Chemistry, University of North Carolina, Chapel Hill, North Carolina 27514, United States*

Adam R. Hall − *Center of BioModular Multiscale Systems for Precision Medicine, The University of Kansas, Lawrence, Kansas 66045, United States; Virginia Tech-Wake Forest University School of Biomedical Engineering and Sciences and Comprehensive Cancer Center, Wake Forest School of Medicine, Winston Salem, North Carolina 27101, United States;* orcid.org/0000-0003-2053-6075

Katie Childers − *Bioengineering Program and Center of BioModular Multiscale Systems for Precision Medicine, The University of Kansas, Lawrence, Kansas 66045, United States*

Taryn McNickle − *Department of Chemistry and Center of BioModular Multiscale Systems for Precision Medicine, The University of Kansas, Lawrence, Kansas 66045, United States*

Shalee Mog − *Department of Chemistry and Center of BioModular Multiscale Systems for Precision Medicine, The University of Kansas, Lawrence, Kansas 66045, United States*

Elaine Yeh − *Department of Chemistry and Center of BioModular Multiscale Systems for Precision Medicine, The University of Kansas, Lawrence, Kansas 66045, United States*

Andrew K. Godwin − *Center of BioModular Multiscale Systems for Precision Medicine, The University of Kansas, Lawrence, Kansas 66045, United States; KU Comprehensive Cancer Center and Kansas Institute for Precision Medicine, University of Kansas Medical Center, Kansas City, Kansas 66160, United States*

Complete contact information is available at: https://pubs.acs.org/10.1021/acs.analchem.3c00855

Author Contributions

[$]S.V., H.W., S.S.T.G.: These authors contributed equally to this work.

Notes

The authors declare no competing financial interest.

■ ACKNOWLEDGMENTS

The authors thank the NIH for financial support of this work (NIH RADx program; NIBIB R01-EB031579; NIBIB P41-EB020594; and P20-GM130423). We also express gratitude to the Tina's Wish Foundation for partial financial support of this work. The authors also acknowledge the KU Nanofabrication Facility (KUNF, P20-GM103638) and the University of Kansas Cancer/Medical Center's Biospecimen Repository Core Facility (NCI: P30-CA168524). We would also like to thank Drs. Steve Wolpe, Bill Turpin, and Jaya Ghosh for helpful discussions during this work, Drs. Allen Greiner and Erin Corriveau and Mr. Brian Koelliker from the Wyandotte Health Department, and Lauren DiMartino and the BRCF staff for consenting patients, organizing collection of samples, and banking.

■ REFERENCES

(1) Shapiro, H. M. *Cytometry, Part A* **2004**, *58A*, 13−20.
(2) Davey, H. M.; Kell, D. B. *Microbiological Reviews* **1996**, *60*, 641−696.

(3) Javanmard, M.; Davis, R. W. *Sensors Actuators B: Chem.* **2011**, *154*, 22−27.
(4) Javanmard, M.; Emaminejad, S.; Dutton, R. W.; Davis, R. W. *Anal. Chem.* **2012**, *84*, 1432−1438.
(5) Emaminejad, S.; Javanmard, M.; Dutton, R. W.; Davis, R. W. *Lab Chip* **2012**, *12*, 4499−4507.
(6) Emaminejad, S.; Javanmard, M.; Dutton, R. W.; Davis, R. W. *Anal. Chem.* **2012**, *84*, 10793−10801.
(7) Song, Y.; Zhang, J.; Li, D. *Micromachines* **2017**, *8*, 204.
(8) van der Pol, E.; Coumans, F.A.W.; Grootemaat, A.E.; Gardiner, C.; Sargent, I.L.; Harrison, P.; Sturk, A.; van Leeuwen, T.G.; Nieuwland, R. *Journal of Thrombosis and Haemostasis* **2014**, *12*, 1182−1192.
(9) Haque, F.; Li, J.; Wu, H.-C.; Liang, X.-J.; Guo, P. *Nano Today* **2013**, *8*, 56−74.
(10) Ying, Y.-L.; Cao, C.; Long, Y.-T. *Analyst* **2014**, *139*, 3826−3835.
(11) Davenport, M. W.; Healy, K.; Pevarnik, M.; Teslich, N.; Cabrini, S.; Morrison, A.; Siwy, Z. S.; Létant, S. E. *Biophys. J.* **2013**, *104*, 521a.
(12) DeBlois, R. W.; Wesley, R. K. *J. Virol.* **1977**, *23*, 227−233.
(13) Zhou, K.; Li, L.; Tan, Z.; Zlotnick, A.; Jacobson, S. C. *J. Am. Chem. Soc.* **2011**, *133*, 1618−1621.
(14) Karawdeniya, B. I.; Bandara, Y. M. N. D. Y.; Khan, A. I.; Chen, W. T.; Vu, H.-A.; Morshed, A.; Suh, J.; Dutta, P.; Kim, M. J. *Nanoscale* **2020**, *12*, 23721−23731.
(15) Saleh, O. A.; Sohn, L. L. *Nano Lett.* **2003**, *3*, 37−38.
(16) Amarasekara, C. A.; Athapattu, U. S.; Rathnayaka, C.; Choi, J.; Park, S.; Soper, S. A. *Electrophoresis* **2020**, *41*, 1627.
(17) Harms, Z. D.; Mogensen, K. B.; Nunes, P. S.; Zhou, K.; Hildenbrand, B. W.; Mitra, I.; Tan, Z.; Zlotnick, A.; Kutter, J. P.; Jacobson, S. C. *Anal. Chem.* **2011**, *83*, 9573−9578.
(18) Fraikin, J.-L.; Teesalu, T.; McKenney, C. M.; Ruoslahti, E.; Cleland, A. N. *Nat. Nanotechnol.* **2011**, *6*, 308−313.
(19) Becker, H. *Lab Chip* **2009**, *9*, 2759−2762.
(20) Nagura-Ikeda, M.; Imai, K.; Tabata, S.; Miyoshi, K.; Murahara, N.; Mizuno, T.; Horiuchi, M.; Kato, K.; Imoto, Y.; Iwata, M. *J. Clin. Microbiol.* **2020**, *58*, e01438-20.
(21) Zhao, Z.; Vaidyanathan, S.; Bhanja, P.; Gamage, S.; Saha, S.; McKinney, C.; Choi, J.; Park, S.; Pahattuge, T.; Wijerathne, H.; Jackson, J. M.; Huppert, M. L.; Witek, M. A.; Soper, S. A. *Electroanalysis* **2022**, *34*, 1961.
(22) Wijerathne, H.; Witek, M. A.; Jackson, J. M.; Brown, V.; Hupert, M. L.; Herrera, K.; Kramer, C.; Davidow, A. E.; Li, Y.; Baird, A. E.; Murphy, M. C.; Soper, S. A. *Nature Communications Biology* **2020**, *3*, 613.
(23) Pahattuge, T. N.; Jackson, M.; Digamber, R.; Wijerathne, H.; Brown, V.; Witek, M. A.; Perera, C.; Givens, R. S.; Peterson, B. R.; Soper, S. A. *Chem. Commun.* **2020**, *56*, 4098−4101.
(24) Manoharan, A.; Choi, J.; Rathnayaka, C.; Vietz, C.; Shiri, F.; Murphy, M. C.; Park, S.; Soper, S. A. *Lab Chip* **2022**, submitted for publication.
(25) Vaidyanathan, S.; Weerakoon-Ratnayake, K. M.; Uba, F. I.; Hu, B.; Kaufman, D.; Choi, J.; Park, S.; Soper, S. A. *Lab Chip* **2021**, *21*, 1579−1589.
(26) Jackson, J. M.; Witek, M. A.; Kamande, J. W.; Soper, S. A. *Chem. Soc. Rev.* **2017**, *46*, 4245−4280.
(27) Shakeri, A.; Jarad, N. A.; Khan, S.; Didar, T. F. *Anal. Chim. Acta* **2022**, *1209*, 339283.
(28) Choi, J.; Jia, Z.; Riahipour, R.; McKinney, C. J.; Amarasekara, C. A.; Weerakoon-Ratnayake, K. M.; Soper, S. A.; Park, S. *Small* **2021**, *17*, 2102567.
(29) Weatherall, E.; Willmott, G. R. *J. Phys. Chem. B* **2015**, *119*, 5328−5335.
(30) Menestrina, J.; Yang, C.; Schiel, M.; Vlassiouk, I.; Siwy, Z. S. *J. Phys. Chem. C* **2014**, *118*, 2391−2398.
(31) Ghatak, S.; Khona, D. K.; Sen, A.; Huang, K.; Jagdale, G.; Singh, K.; Gopalakrishnan, V.; Cornetta, K. G.; Roy, S.; Khanna, S.; Baker, L. A.; Sen, C. K. *Sci. Rep.* **2021**, *11*, 21723.
(32) Song, Y.; Song, J.; Wei, X.; Huang, M.; Sun, M.; Zhu, L.; Lin, B.; Shen, H.; Zhu, Z.; Yang, C. *Anal. Chem.* **2020**, *92*, 9895−9900.
(33) Chai, Z.; Guo, L.; Jin, H.; Li, Y.; Du, S.; Shi, Y.; Wang, C.; Shi, W.; He, J. *Organic & Biomolecular Chemistry* **2019**, *17*, 2403−2412.
(34) Pahattuge, T. N.; Jackson, J. M.; Digamber, R.; Wijerathne, H.; Brown, V.; Witek, M. A.; Perera, C.; Givens, R. S.; Peterson, B. R.; Soper, S. A. *Chem. Commun.* **2020**, *56*, 4098−4101.
(35) Gamage, S. S. T.; Pahattuge, T.; Wijerathne, H.; Childers, K.; Vaidyanathan, S.; Athapattu, U. S.; Zhang, L.; Zhao, Z.; Hupert, M. L.; Muller, R. M.; Muller-Cohn, J.; Geisbrecht, B. V.; Pathak, H.; Pessetto, Z.; Gan, G.; Choi, J.; Park, S.; Godwin, A. K.; Witek, M. A.; Soper, S. A. *Science Advances* **2022**, *8*, eabn9665.
(36) Mina, M. J.; Parker, R.; Larremore, D. B. *New Engl. J. Med.* **2020**, *382*, 1−3.
(37) Chen, Y. W.; Wang, H.; Hupert, M.; Soper, S. A. *Analyst* **2013**, *138*, 1075−1083.
(38) Chen, Y. W.; Wang, H.; Hupert, M.; Witek, M.; Dharmasiri, U.; Pingle, M. R.; Barany, F.; Soper, S. A. *Lab Chip* **2012**, *12*, 3348−3355.
(39) Pahattuge, T. N.; Freed, I. M.; Hupert, M. L.; Vaidyanathan, S.; Childers, K.; Witek, M. A.; Weerakoon-Ratnayake, K.; Park, D.; Kasi, A.; Al-Kasspooles, M. F.; Murphy, M. C.; Soper, S. A. *ACS Sensors* **2021**, *6*, 1831−1839.

https://doi.org/10.1021/acs.analchem.3c00855
Anal. Chem. 2023, 95, 9892−9900